



Full Length Article

Heterogeneous molecular packing and water effects on the mechanical behaviour of silk-inspired β -sheet crystallites: A steered molecular dynamics study

Cem Uguz ^{a,c} , Ünsal Akdere ^a, Çetin Taşseven ^{a,b,*}

^a Department of Physics, Faculty of Science and Letter, Yıldız Technical University, Davutpaşa Campus, İstanbul 34210, Turkey

^b Physics, Faculty of Science, University of East Anglia, Norwich Research Park, Norwich NR4 7TJ, United Kingdom

^c Laboratory for Innovative Drugs (Lab4IND), Computational Design Center (HITMER), Bahçeşehir University, 34734 İstanbul, Turkey

ARTICLE INFO

Keywords: β -sheet crystals

Steered molecular dynamics

Mechanical behavior

Packing heterogeneity

Water effect

ABSTRACT

Bombyx-mori silk fibroin (SF) features outstanding mechanical properties, arising from its β -sheet content. This study investigates the effect of heterogeneous molecular packing and water environment on the mechanical behaviour of silk-inspired β -sheet crystallites using steered molecular dynamics (SMD) simulation technique. Two distinct antipolar antiparallel crystallite models were constructed based on experimental Silk II structures, differing intermolecular packing arrangements, instead of widely used highly ordered theoretical model of β -sheet structure. Results of pull-out simulations of six different β -chains reveal that heterogeneous molecular packing introduces location-dependent mechanical strength, which cannot be predicted based on chain region (core vs. surface) only. Water selectively weakens the surface and corner chains while either ineffective or slightly enhances the strength via hydrogen bond bridges formed prior to ultimate rupture. It also smoothes the stick-slip motion and expedites complete dissociation. Our finding provides atomistic insights into structure–mechanical relationship silk fibroin and highlight the critical role of packing heterogeneity and aqueous environment in tuning silk-based materials for biomedical and engineering applications.

1. Introduction

Bombyx mori (*B. mori*) silk fibroin (SF), a natural semi-crystalline composite biopolymer, is a promising material extensively used in various areas of applications. Beyond its traditional usage in textile industry [1,2] and mechanical engineering [3–5], SF is also highly favoured in biomedical sciences where biocompatibility, biodegradability as well as mechanical superiority are the essential factors [6,7]. During the pupal stage, silkworm develop SF with remarkable structural functionality and properties that outperform most biomaterial competitors, offering protection from predators and external conditions. Multidomain structure of SF composed of a heavy chain (HC) (~350 kDa) covalently linked via disulfide bonds to a light chain (~60 kDa), with non-covalently associated P25 (~25 kDa). The HC's primary structure includes 12 repetitive domains connected by 11 less ordered turns, forming β -sheets. Its amino acid composition primarily consists of

Glycine (45.9 %), Alanine (30.3 %), Serine (12.1 %), and Tyrosine (5.3 %). The molecular design of β -sheet crystallites is characterized by the (Gly-X) dipeptide motif, with significant contributions from Alanine (~65 %), Serine (~23 %), Tyrosine (~12 %), and Valine (~5%). These crystallites are embedded in an amorphous matrix and aligned during the natural spinning process, resulting in high tensile strength and thermal stability. Meanwhile, the amorphous regions contribute to its exceptional extensibility [7–10]. SF stands out among its natural and synthetic counterpart fibers due to its exceptional toughness and strength-stronger than steel wire and comparable to Kevlar in mechanical performance. Additionally, SF exhibits other unique protective functions and properties such as hygroscopicity, thermal insulation, and regulation of gas diffusion [7,10]. Extensive research has explored the factors affecting silk fibers' mechanical performance and their relationship to molecular structure and design. Key findings indicate that: the size, orientation, and β -sheet crystallite content play a crucial role in

* Corresponding author at: Department of Physics, Faculty of Science and Letter, Yıldız Technical University, Davutpaşa Campus, İstanbul 34210, Turkey.
E-mail address: tasseven@yildiz.edu.tr (C. Taşseven).

¹ This research was partly conducted on sabbatical leave of corresponding author at the University of East Anglia: Physics, Faculty of Science, University of East Anglia, Norwich Research Park, Norwich NR4 7TJ, United Kingdom.

determining the mechanical properties; hydration and metal infiltration significantly affect performance; reducing β -sheet crystalline size and alignment along the fiber direction enhance strength; faster reeling speeds and initial stretching improve interlocking regions and durability; artificially accelerated spinning improves tensile properties and thermal stability; hot stretching enhances β -sheet nanocrystal content and orientation boosting mechanical properties; spider silk retains toughness and extensibility below 0 °C; Bombyx mori silk remains stable up to 423–500 K but becomes amorphous at 570 K, with tensile strength decreasing beyond 400 K; incorporating silk fibers into synthetic fibers increases modulus but decreases tensile strength due to bonding breakdown; and both the amorphous region and the crystallites exhibit similar stress but different strain in series combination [3,11–19].

Molecular dynamics (MD) simulations have advanced our understanding of mechanical of silk-based materials. Studies on silkworm and spider silk have examined the mechanical responses and failure mechanisms of pure β -sheet crystalline segments [20–25], and the hybrid crystalline-amorphous system via variety of mechanical test simulations [26–33]. Pull-out and shear deformation simulations have revealed that nanoconfinement, a phenomenon characterized by dissipative molecular stick-slip deformation and uniform shear deformation, significantly enhances the mechanical properties of crystallites. β -sheet crystals with smaller cross-sectional areas, comprising fewer β -strands, exhibit superior stiffness, strength, and toughness compared to their larger counterparts [23]. Studies on models of Clavipes spider dragline silk constructed with two amorphous domains connected by the terminal residues of a single β -sheet crystallite have analysed the deformation mechanisms at atomistic level to demonstrated the role of structural organization in determining mechanical behaviour [32,33]. Mechanical pull-out tests on pure β -sheet crystallites confirmed that both stick-slip and uniform shear deformations are predominantly governed by hydrogen bonding between β -strands [22,23]. Water content significantly alters the intermolecular interactions, which weakens the strength of the β -sheets [23]. The effects of tensile loading and water concentration have been examined on Bombyx mori silk fibroin via constructing four distinct nanostructural models, each consists of eight β -sheet crystallites connected by amorphous regions [29,30]. It has revealed the critical role of water in modulating the mechanical properties of silk. A more realistic atomistic network model of silk fibroin, which incorporates both β -sheet crystallites and amorphous domains, has been developed providing deeper insights into stress distribution across secondary structures during mechanical loading [31]. A study on independent mechanical behaviours of crystalline and amorphous domains based on a model of linear viscoelastic theory coupled with X-ray diffraction demonstrated that β -sheet crystallites not only contribute to the extensibility of silk fibers but also undergo elastic deformation [34]. This revealed the multifunctional role of β -sheet crystallites, which, in addition to acting as cross-linking agents, enhance the extensibility and mechanical performance of silk fibers. Axial loading simulations further revealed anisotropic mechanical response of β -sheet nano-crystallites, akin to polyamide crystallites, forming new hydrogen under strain along chain direction [35]. Investigations on silk-based nanocomposites (e.g., graphene oxide (GO)-SF [36], carbon nanoscroll (CNS)-silk crystallites [37], and silk peptide-graphene substrates [38]) have established the role of interfacial interactions, hydrogen bonding, and hydration in mechanical performance. In another study, a custom generative large-language model has been proposed to develop novel silk sequences. This expands the scope for synthetic silk engineering [39]. Environmental conditions, such as hydration, alcoholic and salt solutions, further modulate the structural and functional properties of SF [9,13,40–45]. Hydration level affects the formation and stability of β -sheet structures, mechanical strength, elasticity, and biodegradability [13,41,42]. Salt solutions, particularly those containing divalent ions like calcium and magnesium, alter solubility, assembly dynamics, and molecular interactions [40,43,45]. These factors are critical for optimizing SF-based materials for biomedical applications such as tissue

engineering, drug delivery, and regenerative medicine.

This study investigates the complex interplay between the heterogeneous molecular packing, hydrogen bonding, and mechanical behaviour in silk-inspired crystallites. Two antipolar antiparallel β -sheets crystallites models with different intermolecular packing arrangements were constructed based on experimentally determined structure. Using steered molecular dynamics (SMD) simulations methodology, pull-out tests conducted separately on six β -strands from core, surfaces and corners analysing the responses in vacuum and aqueous environments.

2. Models and method

2.1. β -sheet crystallite models

Two antipolar antiparallel β -sheet crystallites models with different intermolecular packing arrangements were constructed using the unit cell space group of P_{2_1} based on the initial coordinates and unit cell parameters provided by Asakura et al. [46]. The sequence of Gly-Ala dipeptide were used to form poly [Gly-Ala]_n chains for both antiparallel β -sheet crystallites models, model 1 and model 2, denoted as (GA)₁ and (GA)₂, respectively. It has been proposed that crystalline Silk II, which must be an antipolar packing, is a statistical mixture of these two packing arrangements in a ratio 2:1 [46]. The initial unit cell replicated twice along sheet stacking and h-bond directions, and six times along the chain direction. Four layers of β -sheets were arranged, each consists of four strands of [Gly-Ala]₆, to construct antiparallel β -sheet crystallite samples, in sizes of 18.76 × 18.98 × 41.88 (Å³). Fig. 1-a and b, respectively, illustrates the structure of model crystallites (GA)₁ and (GA)₂, before equilibration simulations developed using VESTA software [47]. The target chains are represented as A and P, corners, B and O, surface middle layers, and J and G, core. The positioning of the side chain methyl group (CH₃) of Ala residues give rise to one important distinction between the packing arrangements of the models contributing to the heterogenous nature of the Silk II structure [46]. In (GA)₁ it is oriented toward the Gly-H α in the space between the pairs of Gly-Ala bonds. In contrast, the methyl groups in (GA)₂ model are shifted by one residue pointing to the centre of Gly-Ala hydrogen bond pairs. Based on NMR chemical shifts and dipolar couplings it was proposed that the models (GA)₁ and (GA)₂ exhibit different heterogeneous packing arrangement with two different antiparallel β -sheet structures [46]. The both models have nonuniformly aligned antiparallel β -chains leading to variations in hydrogen bonding patterns and dipole orientations with antipolar arrangement. The model (GA)₁ exhibits higher heterogeneous and tighter packing while (GA)₂ is more ordered but still heterogenous and less tightly packed.

2.2. Equilibration and steered molecular dynamics (SMD) simulations

All molecular dynamics (MD) simulation were performed using the open-source GROMACS package [48] with CHARMM27 classical molecular mechanics force field [49], which models bonded interactions (bond stretching, angle bending and torsions) and non-bonded interactions (van der Waals and Coulombic). Prior to the equilibration, steepest descent energy minimisation was conducted over 10⁷ iterations with a step size 0.001 ps, until a maximum potential force of <1000.0 kJ mol⁻¹ nm⁻² was achieved. Simulations were performed under the isothermal-isobaric (NPT) ensemble at T = 300 K and P = 1 bar. Temperature and pressure were controlled by the V-rescale thermostat with a coupling time constant 0.1 ps and the C-rescale barostat with pressure coupling parameter 1.0 ps, respectively. Electrostatics interactions were handled via the Verlet cutoff scheme utilized with the Particle Mesh Ewald (PME) method [50] with a 1.0 nm cutoff distance. The periodic boundary conditions were applied in all three directions to minimize the artificial surface effects. All bond vibrations were constrained using a linear constraint solver (LINCS) algorithm [51] in order to set the simulation time step as 1 fs. The equilibrated model crystallites (GA)₁

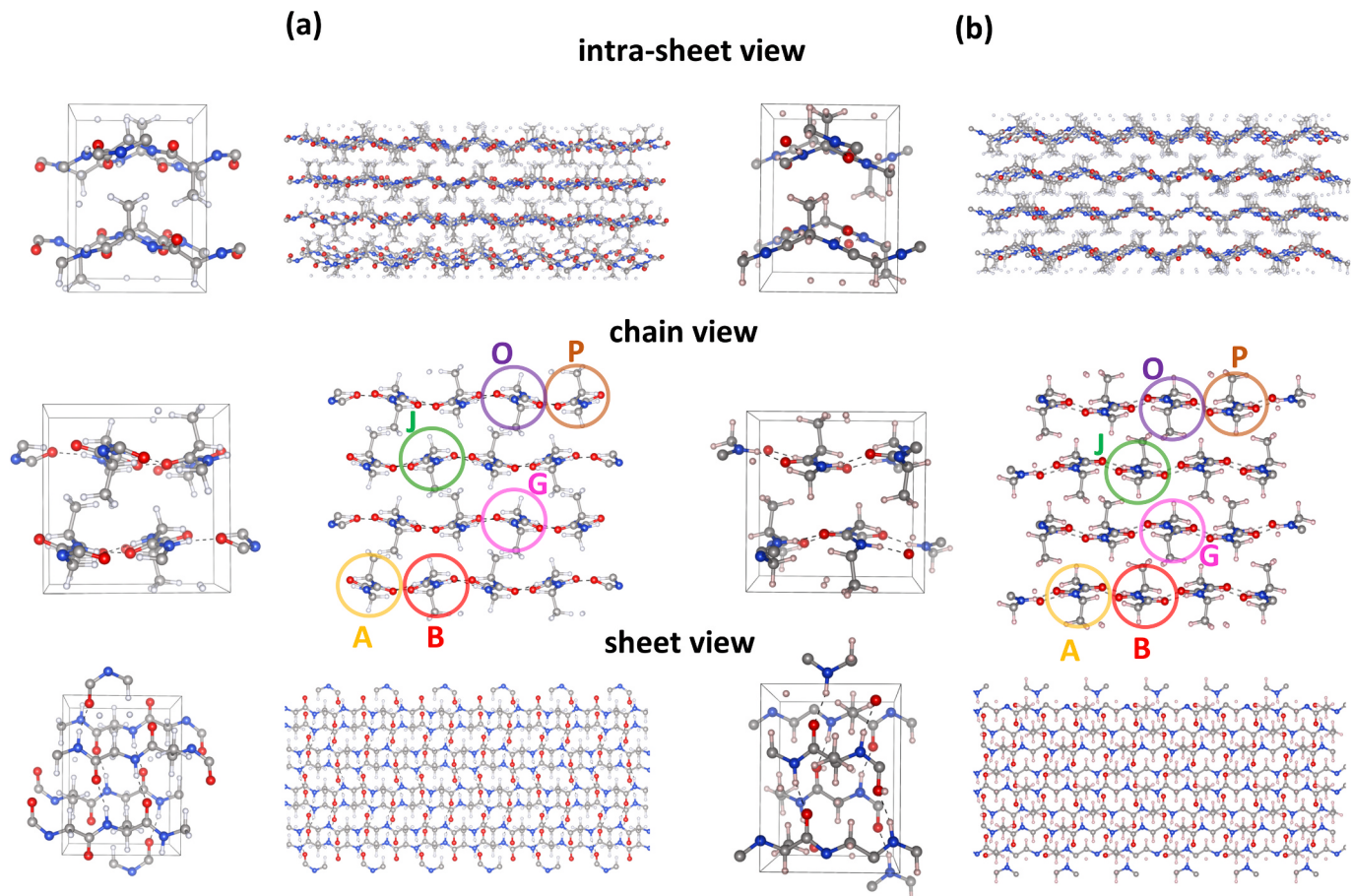


Fig. 1. Crystallite structure of models (a) (GA)₁ and (b) (GA)₂. The first columns show the unit cell and the second columns are the antiparallel beta-sheet crystallites viewed from three orthogonal directions before the equilibrium simulations. Circled strands are the target chains A and P (corners), B and O, (surface layers), and J and G (core region) for pull-out simulations.

and (GA)₂ in vacuum were solvated in a TIP3P water [52] box, with ~75,000 atoms and box size of $6.0 \times 6.5 \times 20.0(\text{nm}^3)$. The resulting equilibrated systems served as starting point for mechanical pull-out simulations in vacuum and in water. The equilibrated structure of crystallites from β -chains view are shown in Fig. 2.

Constant-velocity SMD simulations [53,54] were employed to investigate the mechanical strength of the four different β -sheets crystallite under vacuum and aqueous conditions. Six different chains, located at the core (chain-G and chain-J), surfaces (chain-B and chain-O) and corners (chain-A and chain-P) as shown in Fig. 2, were pulled out from the crystallites. A harmonic bias potential $w(x) = (1/2)k(x(t) - x_0)^2$, where k is the force constant and x_0 is the harmonic potential centre, was applied along the pulling pathway. The primary objective of this study is to examine the mechanical response of the beta-sheet crystallite under a specific pulling rate with a harmonic restraint by means of a single steered MD, not to drive free energy profile, so that, the umbrella sampling (US) [55] was not performed. This method mimics single molecule manipulation experiments like atomic force microscopy (AFM) in force spectroscopy. In SMD simulations, the terminal residue of the target chain was pulled with constant speed v by moving a steered dummy atom attached to the centre of mass of the end of the pulled chain via a virtual spring. The pulling force is given by $F(t) = k(vt - x(t))$, where $x(t)$ is the position of the end of the chain. During this process, all other chains in the crystallite were fixed by an applied counterforce. The target chain was pulled away from the crystallite along the chain direction for 10 ns at 0.001 ps time-step with pulling rate of $v = 0.5 \text{ nm ns}^{-1}$ and a spring constant of $k = 830 \text{ kJ mol}^{-1} \text{ nm}^{-2}$. In total, 24 independent SMD simulations were performed.

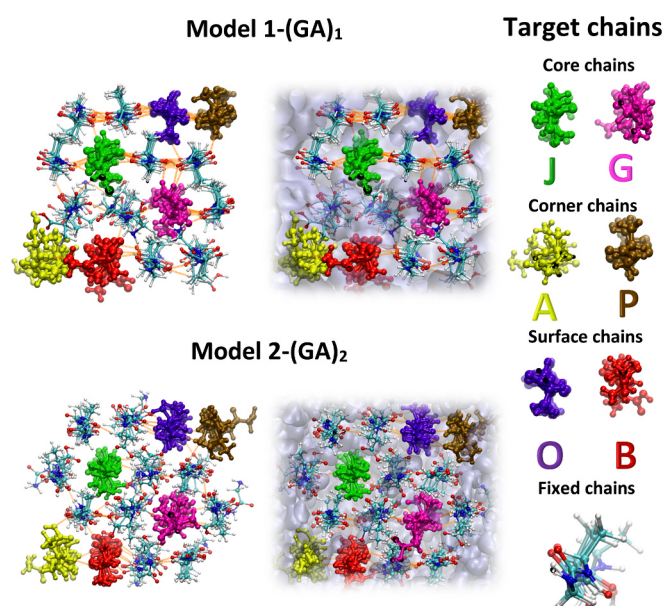


Fig. 2. Equilibrated structure of crystallites from β -chains view and target chains for pull-out simulations.

3. Results and discussions

Previous experimental and theoretical studies have demonstrated that the size, orientation, richness, amino acid sequence of β -sheet crystallites, and environmental conditions (such as hydration, salt solutions, and reeling speed) all significantly influence the mechanical performance of silk fibres. Stretching a silk fiber straightens the amorphous matrix and orients the β -sheet crystallites along the loading direction. The crystallites then take up the load and propagate it through the fiber by forming the interlocking regions, reinforcing the fiber. At large loads, the crystallites fracture through molecular stick-slip and uniform shear deformations [11,23]. Here, we assess the effects of heterogenous inter-sheet packing and aqueous environmental condition on the mechanical response of the two models of antipolar-antiparallel β -sheet crystallites ($(GA)_1$ and $(GA)_2$). For this purpose, the rupture force-displacement and hydrogen bonding calculations were carried out by performing SMD simulations. Fig. 3-a, b, and c show the comparison of the rupture force-displacement behaviour of the pulled chains from the core, surface, and corner of models (GA_1) and (GA_2) in vacuum and water. A total of 24 SMD pull-out tests were performed. This simplified setup captures the complex mechanism of β -sheets crystallites in a stretched fiber and illustrates how molecular packing heterogeneity and water environment affect mechanical response. The snapshots of the rupture mechanism of β -chains are presented in Fig. 4. The core chain-G of both models (Fig. 4-a), and the corner chain-A of model (GA_1) and the surface chain-O of model (GA_2) (Fig. 4-b) are chosen to represent all. Each snapshot shows the instant prior to hydrogen bonds breakage corresponding to the rupture force at peak (Fig. 3), as well as water

molecule diffusion mechanism into the core region during pulling out the chain-G (see also Supplementary materials).

An overview of the mechanical disassociation of process of the target chains from the crystallite can be summarised as follows. Target chains initially exhibit an almost linear response until the ultimate rupture, corresponding to the first hydrogen bond breakage, followed by stick-slip motion and smooth sliding, and finally completely dissociate away from the crystallites. Core chains exhibit local backbone torsion in the part separated from the crystal and then dissociate completely from the crystal without local bending in the direction of pulling. Surface and corner chains reach a more disordered structural state after NPT equilibration compared to middle chains. Due to local weaker interactions (hydrogen bonding and van der Waals) and irregular hydrogen bond distribution, regions near the terminal ends of some chains (chain-A and B in model (GA_1) are bent away from the β -crystallite. Anomalously, corner chain-A in (GA_1) appears to be equilibrated in a partially folded final state. Therefore, when the pulling starts, the target chain first becomes unfolded and then its hydrogen bonds with the crystallite begin to break. In addition to smooth sliding and stick-slip motion, in the case of surface and corner chains, before the terminal end on the pulling side detaches from the crystal, mechanisms such as local detachments along the chain, prior detachment from the opposite end, or straightening of bent regions of the pulled chain can occur. Below, we present a detailed interpretation of the results, and discussions on the disassociation process of target chains from the β -sheets crystallites in the light of inter-sheet packing, heterogeneity, and water environment which influence the rupture mechanics and the hydrogen bonding.

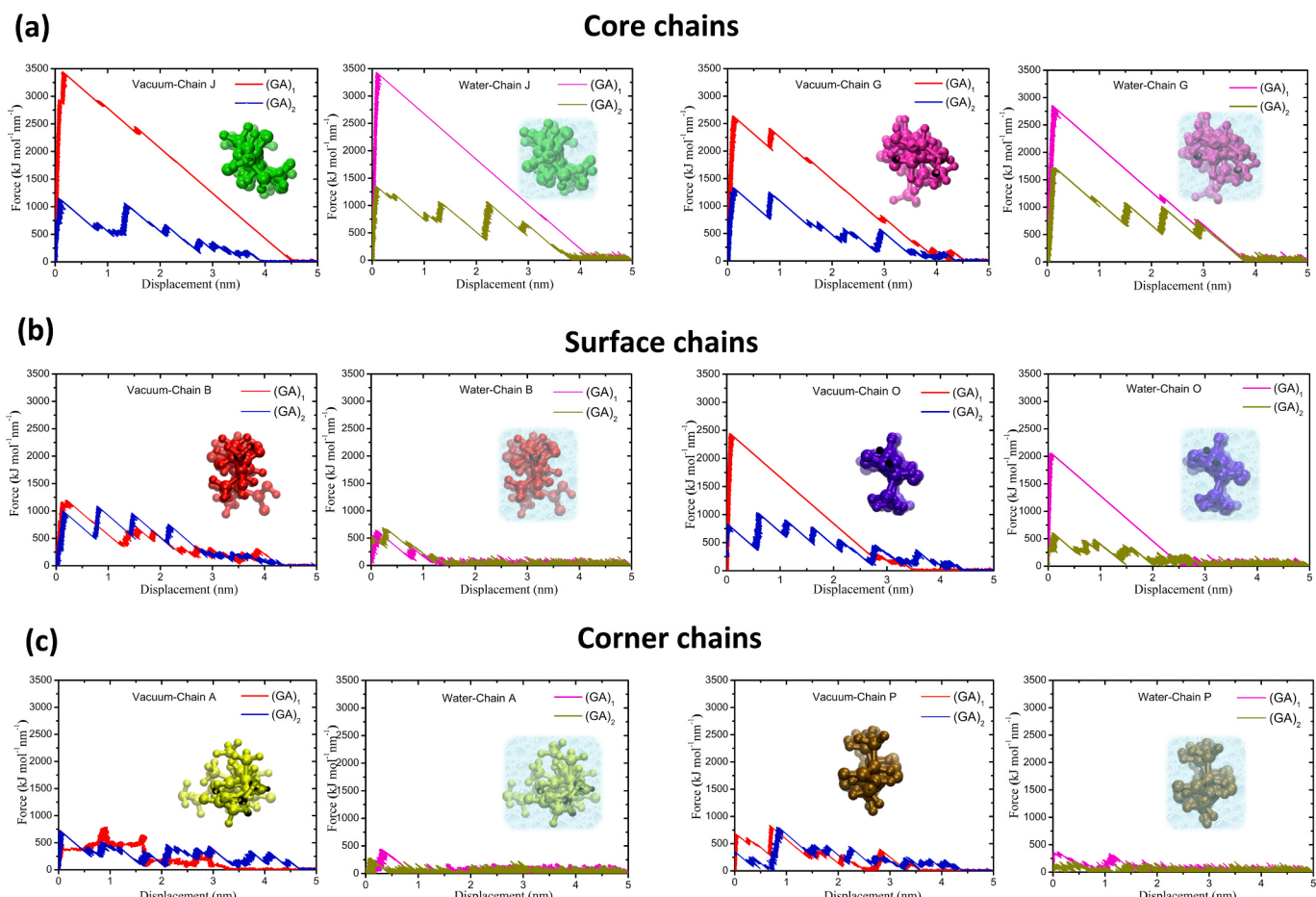


Fig. 3. Force-displacement profile of target chains from (a) core (chain-J and chain-G), (b) surface (chain-B and chain-O), and (c) corner (chain-A and chain-P) regions in model 1-(GA_1) and model 2-(GA_2) obtained from steered molecular dynamics simulations in vacuum and water environments.

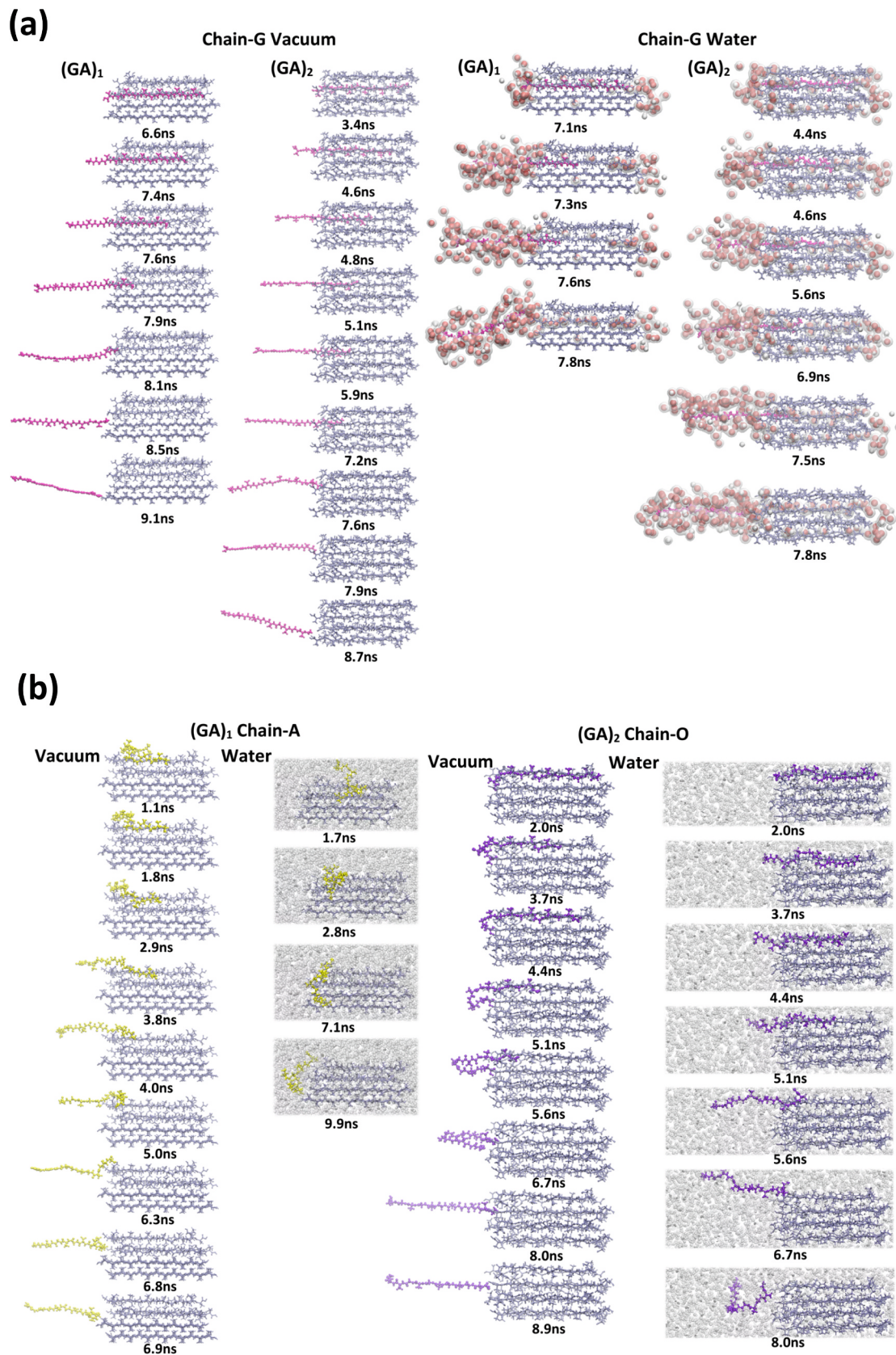


Fig. 4. Snapshots of rupture mechanism of β -cains from different regions of crystallite models in vacuum and water environments. (a) Core chain-G in both models. Water molecules represented with red (oxygen) and white (hydrogen) balls, and only those within 4 Å of the core chains were visualized to highlight the water diffusion into core region. (b) Corner chain-A in $(GA)_1$ and surface chain-O in $(GA)_2$, representing their respective regions and models. Each snapshot captures the instant before hydrogen bond breakage at peak rupture force.

3.1. Rupture mechanics

3.1.1. Elastic region

As is evident from the Fig. 3, during the elastic region of the force–displacement curves, all chains initially exhibit an almost linear response to the applied load until the onset of rupture, corresponding to the first hydrogen bond breakage between the pulled chain and adjacent chains. The ultimate rupture force (URF), defined as the maximum force observed, characterizes the strength of the pulled chains. In the case of the core chains (chain-G and chain-J) and surface chain (chain-O), the URF of $(GA)_1$ model is about 2–3 times greater than that of $(GA)_2$. The difference between the models is considerably reduced when the corner chains chain-A and chain-P, and the surface chain chain-B were pulled out from the crystallites. Another noteworthy finding of this study is that different chains pulled from the same region of the crystallite show different mechanical response against the load both in vacuum and water. Although they are located in the same region, in the core region, chain-J and chain-G, and on the surface region chain-O and chain-B exhibit considerably different strength. Difference in strength between the corner chains chain-A and chain-P is smaller as they are the least interacting chains with crystallites. These highlight the location dependence of the strength of individual chains in the core and surface-mid regions of the β -sheet crystallite reflecting the effect of heterogeneous molecular packing.

Regarding the environmental effect, results show that water does not significantly affect the strength (URF) when pulling core chains. However, it is still necessary to explain the small increase in URF of the middle chains, especially in the G chain. This is due to the initial hydrogen bond bridges formed by water molecules between the terminal residues of the target chain and the adjacent fixed chain. In order to the target chain to start sliding, in addition to the direct hydrogen bonds formed with adjacent fixed chains, the hydrogen bond bridges formed via water molecules must also be broken. Fig. 5-a shows the two types of hydrogen bond bridges $HT1\cdots OW\cdots HT2$ and $OT1\cdots HW2-(OW)\cdots HW1\cdots N$. The bridge $HT1\cdots OW\cdots HT2$ is between the oxygen ion (OW) of a water molecule and the hydrogen ion (HT1) of the terminal glycine residue (Gly) in the fixed chain (blue dashed line: $OW\cdots HT1$), and between the same water oxygen (OW) and the hydrogen ion (HT2) of the terminal alanine residue (Ala) in the target chain (red dashed line). The bridge $OT1\cdots HW2-(OW)\cdots HW1\cdots N$ is between the oxygen ion (OT1) of terminal alanine residue in the target chain and one of the hydrogen ions (HW2) of a water molecule (red dashed line: $OT1\cdots HW2$), and between another hydrogen ion (HW1) of the same water molecule and the nitrogen ion (N) of the terminal glycine residue in the fixed chain (red dashed line: $HW1\cdots N$). These hydrogen bond bridges oppose the applied load to the target core chain, enhancing the strength in water, albeit slightly. In Fig. 5-b the number of hydrogen bond bridges between the target core chain (G and J) and the adjacent fixed chain during the course of pulling simulation is shown. To calculate the hydrogen bonds, the geometrical criteria were employed as the cut-off distance and cut-off angle of 3.5 \AA and 30° , respectively. Following the initial rupture of hydrogen bond bridges, new bridges continue to form between the target chain and the fixed chains via water molecules as the target chain is pulled away from crystallite. Hydrogen bond bridges persistently reform during the pulling, with the chains G and J, respectively, maintaining average of ~ 2.5 and ~ 3.3 bridges on average. As expected, the number of bridges drops to zero after complete dissociation of the target chain from the crystallite.

Conversely, surface and corner chains experience a noticeable weakening in water. Prior studies have shown that water plasticizes the amorphous region enhancing the chain mobility because of disruption of the hydrogen bonding between amorphous molecules and bound water molecules, and induces the β -sheet crystallization [56,57]. Additionally, the stress-strain analysis of silk film has revealed that the mechanical properties does not change significantly up to 84 % of relative humidity, but striking decrease in tensile strength and Young's modulus, along

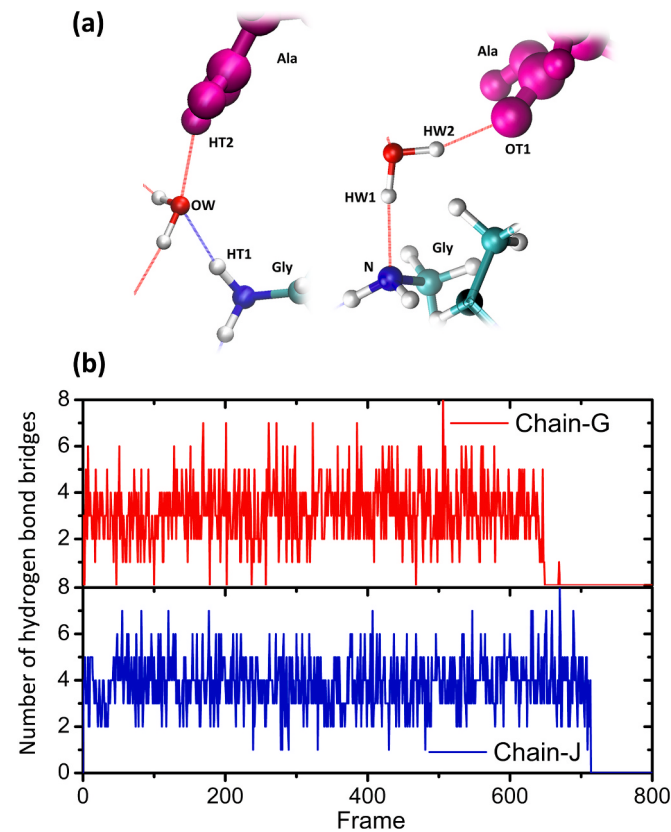


Fig. 5. (a) Two types of hydrogen bond (red and blue dashed lines) bridges are shown: $HT1\cdots OW\cdots HT2$ and $OT1\cdots HW2-(OW)\cdots HW1\cdots N$. Where H, O, N, and W represent hydrogen ion, oxygen ion, nitrogen ion and water molecule, respectively, (b) Number of hydrogen bond bridges between the target core chains (G and J) and the adjacent fixed chain.

with increased elongation at break and toughness, were observed at 97 % humidity [57]. MD simulations of tensile deformation in phenomenological models of *B. mori* SF consisting of interconnected crystalline and amorphous domains have demonstrated that the water environment strengthens SF at low hydration levels but weakens it at high hydration levels [29,30]. A follow-up study reveal that the mechanical response of SF is enhanced in saline environment (water-Na-Cl) [45]. Earlier SMD simulations further showed that water has weakening influence on the strength of the β -sheets crystallite, which was a highly ordered theoretical model, by hindering the hydrogen bond formations [24]. However, force–displacement results from the present SMD simulations suggest that the water environment does not appear to have weakening effect on the strength of crystallites during the pulling of middle chain from the core region. On the contrary, water either does not affect the strength of the middle chains or, as mentioned above, it may even cause a slight increase in strength due to the formation of hydrogen bond bridges between the terminal residues of the pulled chain and the adjacent fixed chain (Fig. 5).

Examination of water diffusion between the β -sheets of the crystallite using the VMD (Visual Molecular Dynamics) software [58] has shown that only a few water molecules can diffuse between the surface layers and core region (Fig. 4 and Supplementary materials). This occurs slightly more in model $(GA)_2$ as it has intrinsically less tightly packed molecular structure than $(GA)_1$. Following ultimate rupture, the chain slides between the sheets leaving an unoccupied linear region behind, and then the water molecules start diffusing into the core region from the opposite side of the crystallite along the chain vacancy (Fig. 4 and Supplementary materials). Unlike what was observed for the middle layer β -chains, water significantly weakens the strength of surface and

corner β -chains due to the greater exposure of water perturbing the formation of hydrogen bonds of surface and corner chains. Although these findings confirm previous SMD study [24], here, we propose that the surface and corner chains are responsible for the weakening of β -sheet crystallite in water, while the core chains either remain unaffected or can have minor enhancing contribution due to the hydrogen bond bridges formed by water molecules between the target chain and fixed chain (Fig. 5). Also note that, the same mechanism of diffusion and interaction of water molecules discussed above have been observed for both $(GA)_1$ and $(GA)_2$ models. The results further indicate that due to the structural heterogeneity, theoretical pull-out tests applied to only one β -chain cannot be decisive on mechanical properties and may be inadequate for comparisons with other synthetic or biomaterials.

3.1.2. Chain-slide region (stick-slip motion)

The elastic region is followed by the development of a new regime where the mechanical disassociation of the target chains proceeds via stick-slip motion reflected, reflected as multiple force jumps in most cases. The heterogeneous molecular packing and environment also influence how the stick-slip deformation develops and progresses. As the pulled chain slides between the adjacent chains, stick-slip deformation is more pronounced in $(GA)_2$, with stronger and more frequent force peaks, indicating a greater tendency for hydrogen bond reformation to resist dissociation compared to that in $(GA)_1$. The stick-slip motion has been also observed in earlier studies for various models of $(GA)_n$ and $(AA)_n$ crystallites [22–24,26]. It has been proposed that force peaks separations correspond to either around 0.75 nm, which occur when the chain simply slides between adjacent chains without rotation and reforms at the next hydrogen bond-ring, or 0.38 nm when the chain rotates and forms new hydrogen bond [23]. However, due to boundary conditions applied on crystallite and unconstrained top and bottom layer, it was not observed in another simulation study [28]. In cases where stick-slip motion is observed in our study, although there exist some force peaks occurred at separations corresponding to about 0.71 nm and 0.38 nm, additional peaks also observed at shorter (particularly in the $(AB)_2$) and longer (chain-O in model $(AB)_1$) distances. The reason for this discrepancy between the earlier study and our findings arises from the distinct differences of intermolecular packing and hydrogen bonding pattern of the β -sheets between 2SLK model and $(GA)_{1,2}$ models. In 2SLK, there is compact β -sheet stacking with minimal structural variation forming a regular, highly ordered and denser hydrogen bonding between adjacent β -strands. Whereas in $(GA)_{1,2}$ models in this study, due to the heterogeneous β -sheet packing the hydrogen bonds are non-uniformly distributed with lower density across the crystallites.

In contrast to model $(GA)_2$, the results also revealed that in model $(GA)_1$ the surface layer middle chain (chain-O) does not undergo stick-slip motion in either vacuum or water until it is completely disassociated from the crystallite. However, chain-B pulled from the opposite surface in $(GA)_1$ slides away from the crystal via stick-slip motion. This also evidently shows the reflection of the heterogeneous structure of the crystallite on the mechanical behavior. In the pull-out simulations performed for other chains, water was observed to interfere the stick-slip motion, particularly in corner chains, reducing the intensity and frequency of force peaks. Though it is weak, water also influences target core chains for the following reasons. After the ultimate rupture water diffusion into space from opposite side and the interaction of water molecules with surface and corner chains cause smaller, but still noticeable, dampening effect. This hinders the formation of new hydrogen bonding and the target chain disassociates from the crystallite by a continuous slide. Force-displacement curves confirm that the difference in inter-sheet molecular packing between the models and crystallite heterogeneity, and water also lead to differences between the target chains' stick-slip motions.

3.1.3. Complete disassociation

Eventually, the force drops to zero corresponding to the complete

disassociation of the pulled chain from the crystallite which also is evidently affected by the environment, molecular packing and heterogeneity of the crystallite. The complete disassociation displacement of middle chains roughly matches the full chain length. Molecular packing and heterogeneity introduce minimal variation, and water does not appear to exert a significant effect. In vacuum, for surface and corners, all target chains of $(GA)_2$ and only chain-B of $(GA)_1$ are completely disassociated from the crystallite at a displacement corresponding to the chain length, while this occurs at significantly shorter displacements for the chains-A, O, and P of $(GA)_1$. Intense interactions between water and surface region hinders the reformation of hydrogen bonds, thereby facilitating the complete disassociation of these chains from the crystallite in water at much shorter displacements approximately between 0.5 nm and 3.0 nm compared to vacuum. Influence of water environment on complete disassociation is most prominently observed in the case of corner chains chain-A and chain-P, and surface chain chain-B. Water almost prevents chain-A from forming new hydrogen bonds, leading to a sharp drop and complete disassociation from the crystallite after a displacement of less than 1 nm for both models. Consequently, these emphasize that while heterogeneous molecular packing and water environment does not critically influence the complete separation of the core chains, corner and surface chains are significantly affected.

3.2. Hydrogen bonding

To gain greater insight into the influence of heterogeneous molecular packing and water environment on the mechanical performance of β -sheets crystallites can be made through a quantitative analysis of formation of hydrogen bonds during pull-out simulations. The total number of hydrogen bond of the crystallites during NPT equilibration (Fig. 6-a) reflects the intrinsic structural stability and the strength difference between $(GA)_1$ and $(GA)_2$. In both models, the water environment causes a decrease of total hydrogen bonds, which mainly arises as a consequence of interactions of water with surface β -sheets, clearly demonstrating the weakening effect of hydration on crystalline strength. Below, we discuss the complex mechanical response of the chains in terms of hydrogen bonding during rupture. Fig. 6-b, c, and d show the variation of the hydrogen bonds during pulling between the target chain and adjacent fixed chains, and the target chain and water molecules for the core region, surface sheets and corners, respectively. A total of six chains, two from each region, were subjected to pulling test in vacuum and water.

3.2.1. Core chains (*J* and *G*)

The core chains (*J* and *G*) (Fig. 6-b) in $(GA)_1$, more tightly packed model, consistently form more hydrogen bonds with adjacent β -chains compared to those in $(GA)_2$, both in vacuum and aqueous environments. Moreover, hydrogen bonds between chain-J and adjacent chains are more than that for chain-G as a result of difference in packing. It was observed that the water environment does not significantly disrupt the hydrogen bond formation of both chains for both models. A few hydrogen bonds formed between the target chains and water molecules in model $(GA)_1$ originate from the terminal residues only. Whereas, in model $(GA)_2$, this is clearly greater because there is more water molecule diffusion into core region due to less tightly packed molecular structure of $(GA)_2$ (Fig. 4 and Supplementary materials). In order for the target chain to start sliding, in addition to the direct hydrogen bonds formed with adjacent fixed chains, the hydrogen bond bridges formed via water molecules must also be broken. This causes a small increase in URF peak of chain-G in water environment. Beyond this point, as the target chain begins sliding, the breakage of hydrogen bonds and bridges are observed as a decrease in number of hydrogen bonds. Furthermore, fluctuations in the number of hydrogen bonds explain the more pronounced and frequent stick-slip motion in model $(GA)_2$ compared to that in $(GA)_1$. The decrease in the number of hydrogen bonds of the chain-G chain in water indicates that the interaction of water with the surface layers also

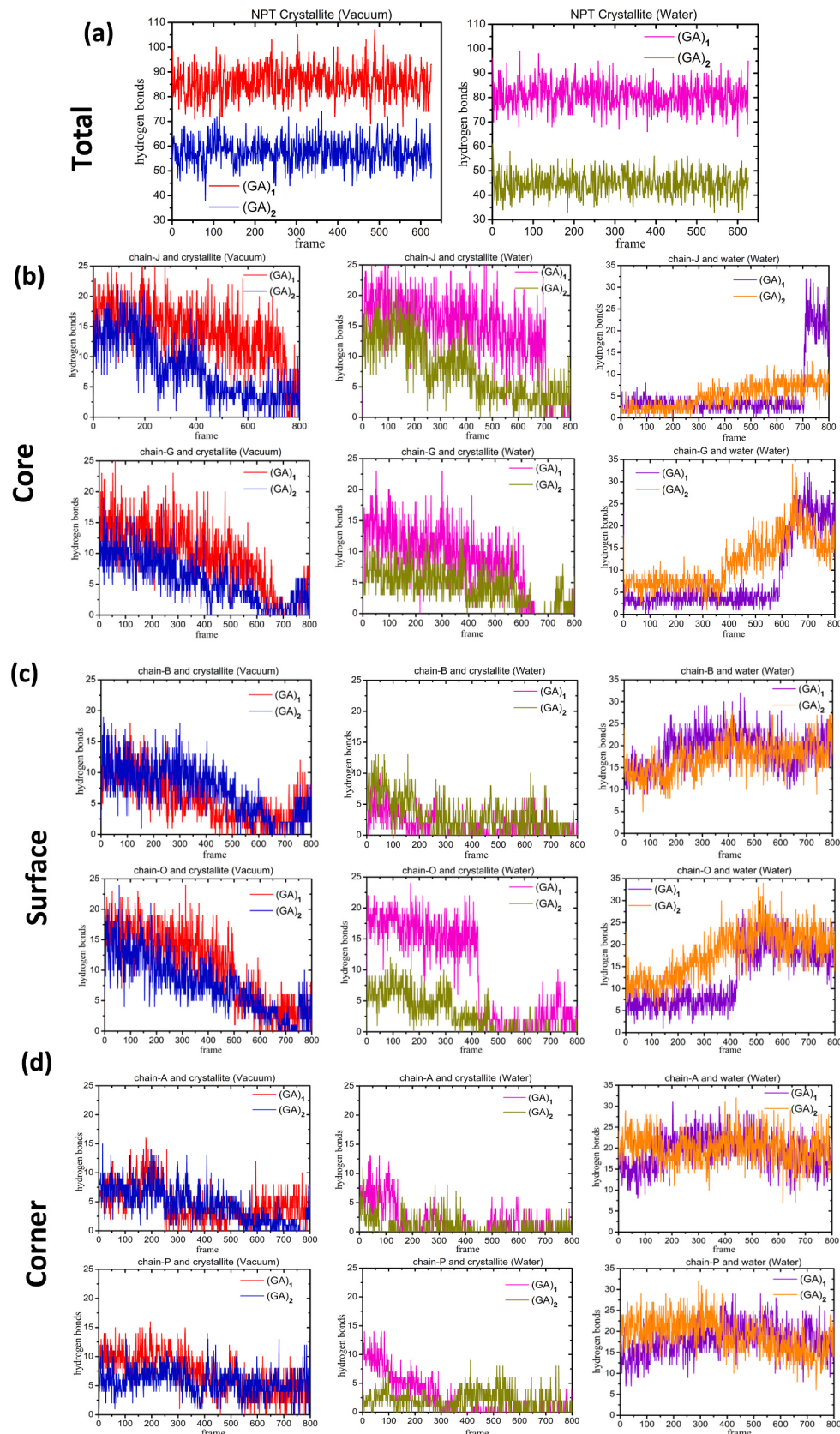


Fig. 6. Evaluation of number of hydrogen bonds for the models (GA)₁ and (GA)₂ in vacuum and water. (a) Total hydrogen bonds between chains in the crystallite during NPT equilibration, and those established by (b) core chains J and G, (c) surface chains B and O, and (d) corner chains A and P.

affects the formation of interchain hydrogen bonds of this chain. This led to a noticeable dampening of the stick-slip motion in the force-displacement curve of chain-G. After complete disassociation, the hydrogen bonding of the chains G and J in $(GA)_A$ and the chain-G in $(GA)_B$ with adjacent chains of crystallite drop to nearly zero in both water and vacuum, while this is not entirely the case for the chain-J chain in $(GA)_B$. This is due to the chain bending and forming intrastrand hydrogen bonds prior to full separation. These differences highlight how local molecular packing and water impact mechanical response of core chains.

3.2.2. Surface chains (O and B)

In vacuum, the hydrogen bonding of the surface chain O with the crystal differs between the $(GA)_1$ and $(GA)_2$ models until complete dissociation, while chain-B displays initially similar bonding that later diverges due to fluctuations in the $(GA)_2$. This causes the $(GA)_1$ and $(GA)_2$ models to show different strengths for the chain-O chain but similar for the chain-B, and the chains O and B to show similar strengths for the $(GA)_2$ as seen in Fig. 3-b. Here too, after ultimate rupture, particularly in $(GA)_2$, fluctuations in hydrogen bond numbers result in mechanical stick-slip motion. Contrary to the general trend, following the first hydrogen bonding breakage, the B chain in $(GA)_2$ forms a few more hydrogen bonds than in $(GA)_1$, resulting slightly higher strength in vacuum and water.

3.2.3. Corner chains (A and P)

Corner chains (A and P) (Fig. 6-c) are the least interacting chains with crystallite; therefore, they form the fewest hydrogen bonds with adjacent chains and exhibit the weakest strength compared to surface and core chains. In vacuum, they show small-scale differences until the first hydrogen bond breakage in both models and then follow a similar stick-slip guideline until complete dissociation. Fluctuations in the number of hydrogen bonds in chains A and P indicate a pronounced stick-slip type motion. Being the most exposed to the aqueous environment, these chains form the greatest number of hydrogen bonds with water molecules, and the most prominent effect of water is observed on them. As seen in the force-displacement behaviour (Fig. 3-c), the reformation of hydrogen bonds following the initial rupture is partially of completely hindered by water. Therefore, the force drops to zero at very small displacement compared to the chain length, leading to complete disassociation from the crystal. Although there are minor differences in detail, from a broader perspective, since these chains interact the least with the crystal, molecular packing and structural heterogeneity cause minimal variation in their mechanical responses.

Perhaps one of the most intriguing findings here is that the number and guideline of hydrogen bonds for the surface chain chain-O and core chain chain-G chain in both $(GA)_1$ and $(GA)_2$ are very similar. Consequently, despite being located in different regions, the surface chain is able to exhibit similar strength and dissociation mechanism as the core chain does. More importantly, this contradicts earlier assumptions from previous SMD studies that core chains possess greater strength than surface chains. Our results reveals that this is not the case for all chains as a result of heterogeneous nature of the crystallite. The main reason for this difference lies in the difference of molecular arrangements between the model crystallites used in the previous [24] and present studies. 2SLK model used in their SMD calculations represents an idealized, highly ordered β -sheet structure with tight packing and uniform hydrogen bonding. It provides a theoretical, simplified model of β -sheet crystallites of poly(Gly-Ala) peptide. Whereas, here we have constructed the models $(GA)_1$ and $(GA)_2$ β -sheet crystallites based on an experimentally validated structure of $(Ala-Gly)_{15}$ peptides, forming antiparallel β -sheets with a heterogeneous packing arrangement [asakura]. They exhibit heterogeneous crystallinity, with alternating highly ordered and slightly disordered β -strands and a more realistic representation of silk fibroin, where structural disorder contributes to mechanical properties like elasticity and toughness.

4. Conclusions

We investigate the effects of heterogenous molecular packing and aqueous environments on the mechanical response of silk-inspired β -sheet crystallites using steered molecular dynamics (SMD) simulations. Crystalline Silk II, believed to exhibit antipolar packing, is proposed to be a statistical mixture of these two packing types in a 2:1 ratio. Models of $(GA)_1$ and $(GA)_2$ β -sheet crystallites have been constructed based on an experimentally validated structure of $(Ala-Gly)_{15}$ peptides, forming antiparallel β -sheets with a heterogeneous packing arrangement characteristic of real silk crystallite. In contrast, 2SLK model widely used in earlier SMD simulation studies represents a theoretically idealized, highly ordered β -sheet structure with tight packing and uniform hydrogen bonding. Pull-out simulations of six different chains from core, surface, and corner regions were performed in both vacuum and water.

Present study reveals that both molecular packing heterogeneity and environmental factors such as hydration critically influence the mechanical behavior of silk-inspired β -sheet crystallites. Two experimentally motivated antipolar antiparallel β -sheet models demonstrated that heterogeneous packing introduces location-dependent mechanical strength, which cannot be predicted solely based on chain region (core vs. surface). Water exposure selectively weakened surface and corner regions while leaving core structures relatively unaffected until post-rupture water diffusion into core region and breakage of hydrogen bond bridges formed by water molecules between the terminal residues of target chains and fixed chains. Hydrogen bonding analyses further emphasized the crucial role of local structure and intermolecular interactions. These findings underscore the necessity of considering packing disorder and environmental effects (e.g., hydrogen bond bridges and regional influence) when designing silk-based materials for high-performance applications in biomedicine and engineering.

CRediT authorship contribution statement

Cem Uguz: Visualization, Software, Data curation. **Ünsal Akdere:** Software, Methodology. **Çetin Taşseven:** Writing – review & editing, Writing – original draft, Methodology.

Declaration of competing interest

The authors declare that they have no known competing financial interests or personal relationships that could have appeared to influence the work reported in this paper.

Acknowledgments

ÇT gratefully acknowledges the sabbatical support between September 2023 and August 2024 by the Yildiz Technical University and the hosting by the University of East Anglia.

Appendix A. Supplementary material

Supplementary data to this article can be found online at <https://doi.org/10.1016/j.commatsci.2025.114053>.

Data availability

The simulation data generated in this study are available from the corresponding author upon reasonable request due to its size.

References

- [1] M.Y. Li, Y. Zhao, T. Tong, X.H. Hou, B.S. Fang, S.-Q. Wu, X.-Y. Shen, H. Tong, Study of the degradation mechanism of Chinese historic silk (*Bombyx mori*) for the purpose of conservation, Polym. Degrad. Stab. 98 (3) (2013) 727–735, <https://doi.org/10.1016/j.polymdegradstab.2012.12.021>.

- [2] N.Y. Dang, W. Ma, S.F. Zhang, B.T. Tang, J.Z. Yang, Studies on anti-wrinkle properties of silk fabrics dyed with reactive and crosslinking dyes, *Text. Res. J.* 80 (4) (2010) 374–382, <https://doi.org/10.1177/0040517509340598>.
- [3] M.-p. Ho, K.-t. Lau, H. Wang, D. Bhattacharyya, Characteristics of a silk fibre reinforced biodegradable plastic, *Compos. B Eng.* 42 (2) (2011) 117–122, <https://doi.org/10.1016/j.compositesb.2010.10.007>.
- [4] Q. Liu, X. Wang, Y. Zhou, Y. Li, Z. Peng, Z. Tang, X. Cai, X. Fan, X. Tang, X. Tan, X. Xie, X. Li, Z. Dong, P. Zhao, Q. Xia, Fe-reinforced silkworm silk with superstrong mechanical properties for mass production, *Chem. Eng. J.* 496 (2024) 153613, <https://doi.org/10.1016/j.cej.2024.153613>.
- [5] R.R. Jose, R. Elia, L.W. Tien, D.L. Kaplan, Electroresponsive aqueous silk protein as “Smart” mechanical damping fluid, *ACS Appl. Mater. Interfaces* 6 (9) (2014) 6212–6216, <https://doi.org/10.1021/am501242w>.
- [6] R.L. Moy, A. Lee, A. Zalka, Commonly used suture materials in skin surgery, *Am. Fam. Phys.* 44 (6) (1991) 2123–2128.
- [7] C. Vepari, D.L. Kaplan, Silk as a biomaterial, *Prog. Polym. Sci.* 32 (8–9) (2007) 991–1007, <https://doi.org/10.1016/j.progpolymsci.2007.05.013>.
- [8] S. Inoue, K. Tanaka, F. Arisaka, S. Kimura, K. Ohtomo, S. Mizuno, Silk fibroin of Bombyx mori is secreted, assembling a high molecular mass elementary unit consisting of H-chain, L-chain, and P25, with a 6:6:1 molar ratio, *J. Biol. Chem.* 275 (51) (2000) 40517–40528, <https://doi.org/10.1074/jbc.M006897200>.
- [9] L.D. Koh, Y. Cheng, C.P. Teng, Y.W. Khin, X.J. Loh, S.Y. Tee, M. Low, E. Ye, H. D. Yu, Y.W. Zhang, M.Y. Han, Structures, mechanical properties and applications of silk fibroin materials, *Prog. Polym. Sci.* 46 (2015) 86–110, <https://doi.org/10.1016/j.progpolymsci.2015.02.001>.
- [10] A. Reizabal, C.M. Costa, L. Pérez-Álvarez, J.L. Vilas-Vilela, S. Lánceros-Méndez, Silk fibroin as sustainable advanced material: material properties and characteristics, processing, and applications, *Adv. Funct. Mater.* 33 (2023) 2210764, <https://doi.org/10.1002/adfm.202210764>.
- [11] G. Xu, L. Gong, Z. Yang, X.Y. Liu, What makes spider silk fibers so strong? From molecular-crystallite network to hierarchical network structures, *Soft Matter* 10 (13) (2013) 2116–2123. 10.1039/c3sm52845f.
- [12] N. Du, X.Y. Liu, J. Narayanan, L. Li, M.L. Lim, D. Li, Design of superior spider silk: from nanostructure to mechanical properties, *Biophys. J.* 91 (12) (2006) 4528–4535, <https://doi.org/10.1529/biophysj.106.089144>.
- [13] Z. Shao, F. Vollrath, Surprising strength of silkworm silk, *Nature* 418 (6899) (2002) 741, <https://doi.org/10.1038/418741a>.
- [14] M.M. Khan, H. Morikawa, Y. Gotoh, M. Miura, Z. Ming, Y. Sato, M. Iwasa, Structural characteristics and properties of Bombyx mori silk fiber obtained by different artificial forcibly silking speeds, *Int. J. Biol. Macromol.* 42 (3) (2008) 264–270, <https://doi.org/10.1016/j.ijbiomac.2007.12.001>.
- [15] L. Cheng, J. Shao, F. Wang, Z. Li, F. Dai, Strain rate dependent mechanical behavior of B. mori silk, A. assama silk, A. pernyi silk and A. ventricosus spider silk, *Mater. Des.* 195 (2020) 108988, <https://doi.org/10.1016/j.matdes.2020.108988>.
- [16] H. Lu, K. Xia, M. Jian, X. Liang, Z. Yin, M. Zhang, H. Wang, H. Wang, S. Li, Y. Zhang, Mechanically reinforced silkworm silk fiber by hot stretching, *Research (Washington, DC)* (2022) 9854063, <https://doi.org/10.34133/2022/9854063>.
- [17] Y. Yang, X. Chen, Z. Shao, P. Zhou, D. Porter, D.P. Knight, F. Vollrath, Toughness of spider silk at high and low temperatures, *Adv. Mater.* 17 (1) (2005) 84–88. 10.1002/adma.200400344.
- [18] A. Martel, M. Burghammer, R.J. Davies, C. Riekel, Thermal behavior of Bombyx mori silk: evolution of crystalline parameters, molecular structure, and mechanical properties, *Biomacromolecules* 8 (11) (2007) 3548–3556, <https://doi.org/10.1021/bm700935w>.
- [19] J. Sirichaisit, V.L. Brookes, R.J. Young, F. Vollrath, Analysis of structure/property relationships in silkworm (Bombyx mori) and spider dragline (Nephila edulis) silks using Raman spectroscopy, *Biomacromolecules* 4 (2) (2003) 387–394, <https://doi.org/10.1021/bm0256956>.
- [20] M.J. Buehler, S. Keten, Elasticity, strength and resilience: a comparative study on mechanical signatures of α -Helix, β -sheet and tropocollagen domains, *Nano Res.* 1 (2008) 63–71, <https://doi.org/10.1007/s12274-008-8006-7>.
- [21] S. Keten, M.J. Buehler, Geometric confinement governs the rupture strength of H-bond assemblies at a critical length scale, *Nano Lett.* 8 (2) (2008) 743–748, <https://doi.org/10.1021/nl0731670>.
- [22] S. Xiao, W. Stacklies, M. Cetinkaya, B. Markert, F. Gräter, Mechanical response of silk crystalline units from force-distribution analysis, *Biophys. J.* 96 (10) (2009) 3997–4005, <https://doi.org/10.1016/j.bpj.2009.02.052>.
- [23] S. Keten, Z. Xu, B. Ihle, M.J. Beuhler, Nanoconfinement controls stiffness, strength and mechanical toughness of β -sheet crystals in silk, *Nat. Mater.* 9 (2010) 359–367, <https://doi.org/10.1038/nmat2704>.
- [24] Y. Cheng, L.-D. Koh, D. Li, B. Ji, M.-Y. Han, Y.-W. Zhang, On the strength of β -sheet crystallites of Bombyx mori silk fibroin, *J. R. Soc. Interface* 11 (96) (2014) 20140305, <https://doi.org/10.1098/rsif.2014.0305>.
- [25] C. Xu, D. Li, Y. Cheng, M. Lui, Y. Zhang, B. Ji, Pulling out a peptide chain from β -sheet crystallite: propagation of instability of H-bonds under shear force, *Acta Mech. Sin.* 31 (2015) 416–424, <https://doi.org/10.1007/s10409-015-0404-y>.
- [26] A. Nova, S. Keten, N.M. Pugno, A. Redaelli, M.J. Buehler, Molecular and nanostructural mechanisms of deformation, strength and toughness of spider silk fibrils, *Nano Lett.* 10 (7) (2010) 2626–2634, <https://doi.org/10.1021/nl101341w>.
- [27] G. Bratzel, M.J. Buehler, Molecular mechanics of silk nanostructures under varied mechanical loading, *Biopolymers* 97 (6) (2012) 408–417, <https://doi.org/10.1002/bip.21729>.
- [28] M. Cetinkaya, S. Xiao, F. Gräter, Effects of crystalline subunit size on silk fiber mechanics, *Soft Matter* 7 (2011) 8142–8148, <https://doi.org/10.1039/C1SM05470H>.
- [29] M. Patel, D.K. Dubey, S.P. Singh, Phenomenological models of Bombyx mori silk fibroin and their mechanical behavior using molecular dynamics simulations, *Mater. Sci. Eng. A* 108 (2020) 110414, <https://doi.org/10.1016/j.msea.2019.110414>.
- [30] M. Patel, D.K. Dubey, S.P. Singh, Investigations into the role of water concentration on mechanical behavior and nanomechanics of Bombyx mori silk fibroin using molecular dynamics simulations, *J. Mater. Sci.* 55 (2020) 17019–17045, <https://doi.org/10.1007/s10853-020-05249-3>.
- [31] W. Shen, Z. Tang, X. Wu, L. Pan, Y. Cheng, B. Hou, J. Song, W. Chen, B. Ji, D. Li, An atomistic model of silk protein network for studying the effect of pre-stretching on the mechanical performances of silks, *Acta Mech. Sin.* 38 (2022) 222013, <https://doi.org/10.1007/s10409-022-22013-x>.
- [32] S. Keten, M.J. Buehler, Atomistic model of the spider silk nanostructure, *Appl. Phys. Lett.* 96 (15) (2010) 153701, <https://doi.org/10.1063/1.3385388>.
- [33] S. Keten, M.J. Buehler, Nanostructure and molecular mechanics of spider dragline silk protein assemblies, *J. R. Soc. Interface* 7 (2010) 1709–1721, <https://doi.org/10.1098/rsif.2010.0149>.
- [34] I. Krasnov, I. Diddens, N. Hauptmann, G. Helms, M. Ogurreck, T. Seydel, S. Sunari, M. Müller, Mechanical properties of silk: interplay of deformation on macroscopic and molecular length scales, *Phys. Rev. Lett.* 100 (4) (2008) 048104, <https://doi.org/10.1103/PhysRevLett.100.048104>.
- [35] Ç. Taşseven, U. Akdere, S.D. Güney, B. Aksakal, Molecular dynamics modelling of the stress-strain response of β -sheet nanocrystals, *Comput. Mater. Sci.* 246 (2025) 113367, <https://doi.org/10.1016/j.commatsci.2024.113367>.
- [36] X. Zhou, D. Li, S. Wan, Q. Cheng, B. Ji, In silicon testing of the mechanical properties of graphene oxide-silk nanocomposites, *Acta Mech.* 230 (2019) 1413–1425, <https://doi.org/10.1007/s00707-017-2017-y>.
- [37] Y. Cheng, L.-D. Koh, F. Wang, D. Li, B. Ji, J. Yeo, G. Guan, M.-Y. Han, Y.-W. Zhang, Carbon nanoscroll–silk crystallite hybrid structures with controllable hydration and mechanical properties, *Nanoscale* 9 (26) (2017) 9181–9189, <https://doi.org/10.1039/C7NR01428G>.
- [38] Y. Cheng, L.-D. Koh, D. Li, B. Ji, Y. Zhang, J. Yeo, G. Guan, M.-Y. Han, Y.-W. Zhang, Peptide–graphene interactions enhance the mechanical properties of silk fibroin, *ACS Appl. Mater. Interfaces* 7 (39) (2015) 21787–21796, <https://doi.org/10.1021/acsm.5b05615>.
- [39] W. Lu, D.L. Kaplan, M.J. Buehler, Generative modeling, design and analysis of spider silk protein sequences for enhanced mechanical properties, *Adv. Funct. Mater.* 34 (2023) 2311324, <https://doi.org/10.1002/adfm.202311324>.
- [40] I.C. Um, H.Y. Kweon, Y.H. Park, S. Hudson, Structural characteristics and properties of the regenerated silk fibroin prepared from formic acid, *Int. J. Biol. Macromol.* 29 (2) (2001) 91–97, [https://doi.org/10.1016/S0141-8130\(01\)00159-3](https://doi.org/10.1016/S0141-8130(01)00159-3).
- [41] C. Holland, K. Numata, J. Rnjak-Kovacina, F.P. Seib, The biomedical use of silk: past, present, future, *Adv. Healthc. Mater.* 8 (1) (2019) 1800465, <https://doi.org/10.1002/adhm.201800465>.
- [42] D.N. Rockwood, R.C. Preda, T. Yücel, X. Wang, M.L. Lovett, D.L. Kaplan, Materials fabrication from Bombyx mori silk fibroin, *Nat. Protoc.* 6 (10) (2011) 1612–1631, <https://doi.org/10.1038/nprot.2011.379>.
- [43] B. Kundu, R. Rajkhowa, S.C. Kundu, X. Wang, Silk fibroin biomaterials for tissue regeneration, *Adv. Drug Deliv. Rev.* 65 (4) (2013) 457–470, <https://doi.org/10.1016/j.addr.2012.09.043>.
- [44] Y.H. Chiao, W.S. Hung, Separation performance of alcohol-induced silk fibroin membranes with homogeneous and heterogeneous microstructures, *Sep. Purif. Technol.* 293 (2022) 121004, <https://doi.org/10.1016/j.seppur.2022.121004>.
- [45] M. Patel, D.K. Dubey, S.P. Singh, Insights into nanomechanical behavior and molecular mechanisms in Bombyx mori silk fibroin in saline environment using molecular dynamics analysis, *Macromolecules* 29 (2021) 694–712, <https://doi.org/10.1007/s13233-021-9084-6>.
- [46] T. Asakura, T. Ohata, S. Kamei, K. Okushita, K. Yazawa, Y. Nishiyama, K. Nishimura, A. Aoki, F. Suzuki, H. Kaji, A.S. Ulrich, M.P. Williamson, Intermolecular packing in B. mori silk fibroin: multinuclear NMR study of the model peptide (Ala-Gly)15 defines a heterogeneous antiparallel antiparallel mode of assembly in the II form, *Macromolecules* 48 (1) (2015) 28–36, <https://doi.org/10.1021/ma502191g>.
- [47] K. Momma, F. Izumi, VESTA: a three-dimensional visualization system for electronic and structural analysis, *J. Appl. Cryst.* 41 (2008) 653–658, <https://doi.org/10.1107/S0021889808012016>.
- [48] B. Hess, C. Kutzner, D.V.D. Spoel, E. Lindahl, GROMACS 4: algorithms for highly efficient, load-balanced, and scalable molecular simulation, *J. Chem. Theory Comput.* 4 (3) (2008) 435–447, <https://doi.org/10.1021/ct700301q>.
- [49] R.B. Brooks, C.L. Brooks 3rd, A.D. Mackerell Jr, L. Nilsson, R.J. Petrella, B. Roux, Y. Won, G. Archontis, C. Bartels, S. Boresch, A. Cafisch, L. Caves, Q. Cui, A. R. Dinner, M. Feig, S. Fischer, J. Gao, M. Hodoscek, W. Im, K. Kuczera, T. Lazaridis, J. Ma, V. Ovchinnikov, E. Paci, R.W. Pastor, C.B. Post, J.Z. Pu, M. Schaefer, B. Tidor, R.M. Venable, H.L. Woodcock, X. Wu, W. Yang, D.M. York, M. Karplus, CHARMM: the biomolecular simulation program, *J. Comput. Chem.* 30 (10) (2009) 1545–1614, <https://doi.org/10.1002/jcc.21287>.
- [50] T. Darden, D. York, L. Pedersen, Particle mesh Ewald: an $N \log(N)$ method for Ewald sums in large systems, *J. Chem. Phys.* 98 (1993) 10089–10092, <https://doi.org/10.1063/1.464397>.
- [51] B. Hess, H. Bekker, H.J.C. Berendsen, J.G.E.M. Fraaije, LINCS: a linear constraint solver for molecular simulations, *J. Comput. Chem.* 18 (1997) 1463–1472, [https://doi.org/10.1002/\(SICI\)1096-987X\(199709\)18:12<1463::AID-JCC4>3.0.CO;2-H](https://doi.org/10.1002/(SICI)1096-987X(199709)18:12<1463::AID-JCC4>3.0.CO;2-H).
- [52] W.L. Jorgensen, J. Chandrasekhar, J.D. Madura, R. Impey, M.L. Klein, Comparison of simple potential functions for simulating liquid water, *J. Chem. Phys.* 79 (1983) 926–935, <https://doi.org/10.1063/1.445869>.

- [53] M. Sotomayor, K. Schulten, Single-molecule experiments in vitro and in silico, *Science* 316 (2007) 1144–1148, <https://doi.org/10.1126/science.1137591>.
- [54] B. Isralewitz, M. Gao, K. Schulten, Steered molecular dynamics and mechanical functions of proteins, *Curr. Opin. Struct. Biol.* 11 (2001) 224–230, [https://doi.org/10.1016/s0959-440x\(00\)00194-9](https://doi.org/10.1016/s0959-440x(00)00194-9).
- [55] G.M. Torrie, J.P. Valleau, Nonphysical sampling distributions in Monte Carlo free-energy estimation: umbrella sampling, *J. Comput. Phys.* 23 (1977) 187–199, [https://doi.org/10.1016/0021-9991\(77\)90121-8](https://doi.org/10.1016/0021-9991(77)90121-8).
- [56] C. Mo, P. Wu, X. Chen, Z. Shao, The effect of water on the conformation transition of *Bombyx mori* silk fibroin, *Vib. Spectrosc* 51 (1) (2009) 105–109, <https://doi.org/10.1016/j.vibspec.2008.11.004>.
- [57] K. Yazawa, K. Ishida, H. Masunaga, T. Hikima, K. Numata, Influence of water content on the β -sheet formation, thermal stability, water removal, and mechanical properties of silk materials, *Biomacromolecules* 17 (3) (2016) 1057–1066, <https://doi.org/10.1021/acs.biomac.5b01685>.
- [58] W. Humphrey, A. Dalke, K. Schulten, VMD - visual molecular dynamics, *J. Mol. Graphics* 14 (1996) 33–38, [https://doi.org/10.1016/0263-7855\(96\)00018-5](https://doi.org/10.1016/0263-7855(96)00018-5).